ACS Energy LETTERS

http://pubs.acs.org/journal/aelccp

Regulation of Buried Interface through the Rapid Removal of PbI_2DMSO Complex for Enhancing Light Stability of Perovskite Solar Cells

Xing Zhao, Yujie Qiu, Min Wang, Danxia Wu, Xiaopeng Yue, Huilin Yan, Bingbing Fan, Shuxian Du, Yuqing Yang, Yingying Yang, Danni Li, Peng Cui, Hao Huang, Yingfeng Li, Nam-Gyu Park,* and Meicheng Li*

Cite This: *ACS Energy Lett.* 2024, 9, 2659−2669

Read Online

ACCESS | Metrics & More | Article Recommendations | Supporting Information

ABSTRACT: The presence of the detrimental PbI_2 residue at the buried interface negatively affects the photovoltaic performance of perovskite solar cells (PSCs). However, the underlying mechanism involved in the formation and elimination of residual PbI_2 has been rarely investigated, despite its critical significance for high-efficiency and stable PSCs. Here, we investigated the formation and elimination mechanism of residual PbI_2 at the buried interface influenced by citric acid (CA) and found that CA can quickly remove the PbI_2DMSO complex through a competitive adsorption mechanism by forming highly crystallized PbI_2. This promotes the subsequent intercalation of amine cations into the PbI_2 framework by forming a stable perovskite. Consequently, the best-performing target PSC achieves an efficiency of 25.19% (a certified efficiency of 24.64%) and 23% from a 1 cm^2 PSC. Additionally, the target PSC also demonstrates improved light stability after 200 h of UV light soaking by maintaining 94.21% of its initial efficiency compared with only 70.76% for the control PSC.

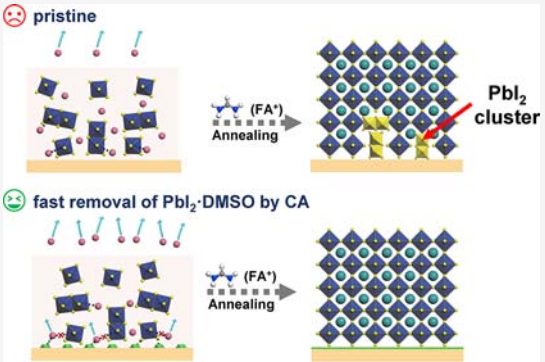

Perovskite solar cells (PSCs) achieve promising photovoltaic performance because of superb light absorption, adjustable band gaps, and easy fabrication process. Since 2012,[1] a variety of strategies, such as material engineering,[2,3] component engineering,[4,5] solvent engineering,[6−8] and interface engineering,[9−12] have been developed to improve the efficiency and stability of PSCs, thereby propelling their commercialization. Recently, a certified efficiency of 26.1% has been reported,[13] which demonstrates the great potential of PSCs in the photovoltaic field. However, because of the fast crystallization process, a large number of defects are inevitably formed inside the perovskite, which influence device efficiency and stability.[14] Residual PbI_2 in perovskite is one of the main defects that exhibits two sides depending on its amount and distribution.[15] A moderate amount of PbI_2 on top of the perovskite can enhance the efficiency because of the passivation effect and the formation of type I band alignment.[16] However, residual PbI_2 at the buried interface undergoes severe photodecomposition accompanied by the formation of deep-level Pb^0 and I_2 traps, which accelerates device degradation, especially under UV light soaking.[17,18]

To eliminate detrimental PbI_2 at the buried interface, interface engineering provides a feasible way to regulate it by introducing external chemical compounds.[19,20] Various interfacial modifiers, such as preburied amine salts[21−24] or coordination compounds,[25−27] have been applied either by consuming the excess PbI_2 or by coordinating with the perovskite. However, how residual PbI_2 is formed at the buried interface and how its elimination is influenced by interfacial modifiers have been rarely studied despite their importance for the enhancement of device efficiency and stability. Among these modifiers, the carboxyl group is commonly used as a

Received: February 5, 2024
Revised: February 27, 2024
Accepted: March 11, 2024
Published: May 10, 2024

https://doi.org/10.1021/acsenergylett.4c00386
ACS Energy Lett. 2024, 9, 2659−2669

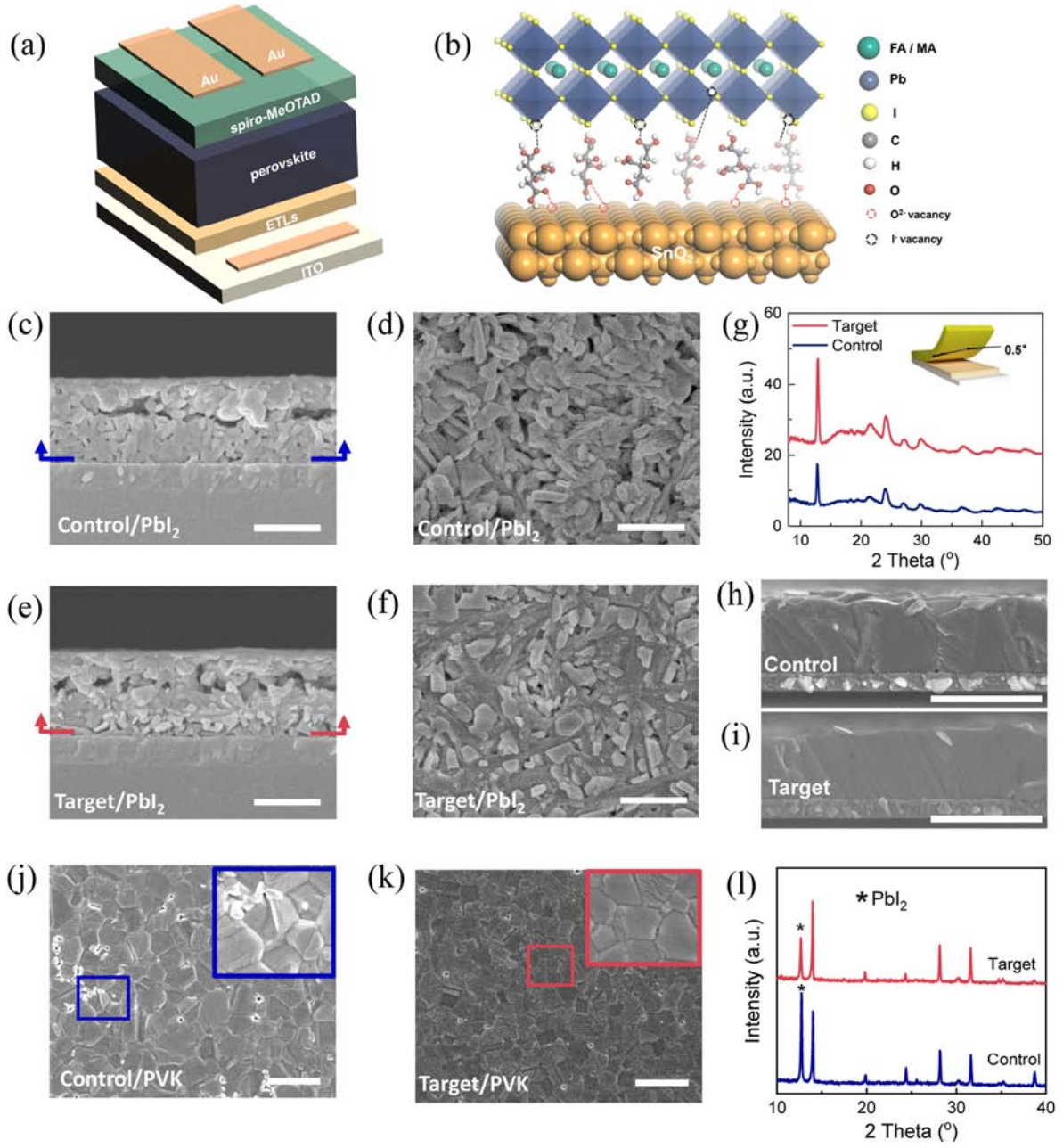

Figure 1. Morphology and crystal structure analysis of PbI_2 and perovskite films. (a) Schematic diagram of the device structure. (b) Possible chemical interaction at the SnO_2/perovskite interface. (c) Cross-sectional SEM image and (d) corresponding bottom surface morphology of the control PbI_2 film. The scale bar is 500 nm. (e) Cross-sectional SEM image and (f) corresponding bottom surface morphology of the target PbI_2 film. The scale bar is 500 nm. (g) GIXRD patterns of PbI_2 films with an incident angle of 0.5°. (h,i) Cross-sectional SEM images of the perovskite films. The scale bar is 1 μm. (j,k) Bottom surface morphologies of perovskite films, and the insertion in each figure shows the locally enlarged image in the rectangle. The scale bar is 2 μm. (l) XRD patterns of the perovskite films.

chemical bridge that can passivate metal oxide and coordinate with Pb^{2+} ion.[28−30] It has also been reported that carboxyl groups are more likely to react with PbI_2 than with amine salts.[31] Therefore, organic acids with carboxyl groups may be good choices for affecting the crystallization process of PbI_2 and better regulating the buried interface.

Here, we investigated the crystal growth mechanism of PbI_2 in the vicinity of the electron transport layer (ETL) influenced by citric acid (CA). We observed that the CA molecule with carboxyl groups can break down the chemical interaction of the PbI_2·DMSO complex, which leads to a fast exfoliation of DMSO. This exfoliation process is highly beneficial for the crystallization of PbI_2, which in turn facilitates the incorporation of amines into its framework, thus enabling the formation of a stable perovskite. As a result, the target device with reduced PbI_2 achieved an efficiency of 25.19%. Moreover, the target PSC also demonstrated good UV light stability compared with the control device. Overall, our findings shed light on efficiently manipulating the residual PbI_2 through the chemical interactions at the buried interface, which provides a new strategy to improve the quality of the buried interface for high-efficiency and stable PSCs.

The PSC with a configuration of ITO/SnO_2/perovskite/spiro-MeOTAD/Au was chosen for this research, as shown in

https://doi.org/10.1021/acsenergylett.4c00386
ACS Energy Lett. 2024, 9, 2659−2669

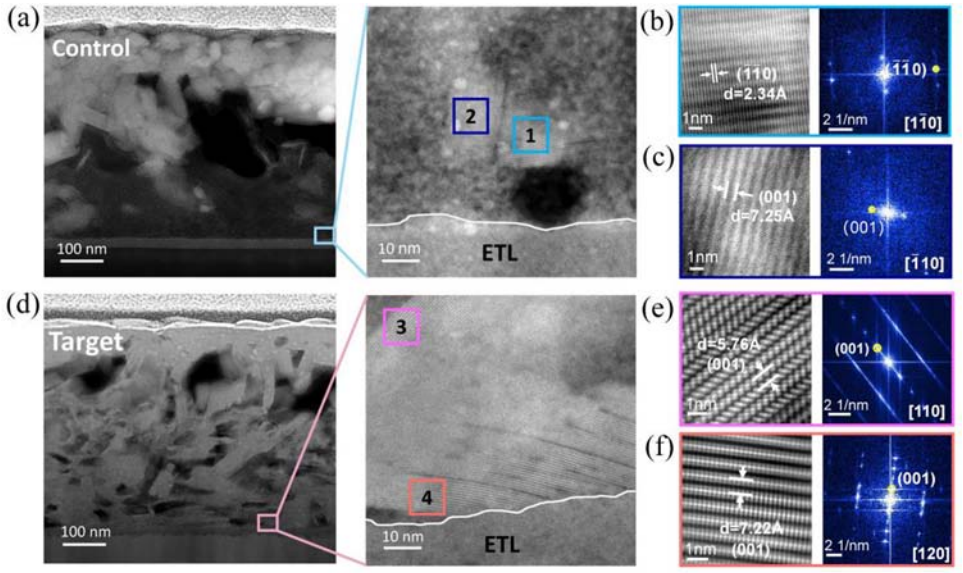

Figure 2. Structural characterization of the as-prepared PbI_2 precursor films. (a) Cross-sectional STEM image of control PbI_2 film with its enlarged view profile. Atomic structure of control PbI_2 of (b) region 1 and (c) region 2. (d) Cross-sectional STEM image of target PbI_2 film with its enlarged view profile. Atomic structure of target PbI_2 of (e) region 3 and (f) region 4.

Figure 1a, and the fabrication process of the PSC can be found in the Supporting Information. To better understand the growth mechanism of PbI_2 at the buried interface and its ultimate influence on device performance, we preferred carboxyl-group-functionalized organic acid because of its good coordination effect. Various organic acids with different numbers of acetic acid groups are illustrated in Figure S1. With three acetic acid groups, CA is expected to achieve superior chelating or coordinating ability with Pb^{2+}. Therefore, we selected CA as the modifier to regulate the buried interface. All samples treated without and with CA are labeled as control and target in the following section, respectively. The schematic diagram of the chemical interaction at the buried interface is shown in Figure 1b. The chemical interactions between CA and SnO_2 were first characterized by Fourier transform infrared (FTIR) spectroscopy and X-ray photoelectron spectra (XPS) measurement, as shown in Figure S2 and Figure S3. In Figure S2, the emerging −COOH peak at 1575 cm^{-1} for the target sample confirms the existence of CA. The vibration peak of Sn−O observed at 710 cm^{-1} for the control sample shifted to 698 cm^{-1} for the target sample, which confirms the chemical interaction between $-COO^-$ and SnO_2. Besides, the peak at 1388 cm^{-1} for CA powder relates to the O−C═O symmetric stretching mode, which was shifted to 1390 cm^{-1}, thereby suggesting that CA binds to SnO_2 via deprotonated carboxyl group with bidentate Sn−O−C bond.[32,33] XPS measurements was performed to further characterize the chemical interaction between CA and SnO_2, as shown in Figure S3. The peaks of Sn $3d_{3/2}$ (494.9 eV) and Sn $3d_{5/2}$ (486.5 eV) observed for the control sample slightly red shifted to 494.8 and 486.4 eV for the target sample because of the increased electron density around the Sn atom.[26,29] The corresponding contact angle and transmission electron microscopy (TEM) images are shown in Figures S4 and S5. In Figure S4, the contact angles of the PbI_2 precursor deposited on control and target ETL substrates are 12.2° and 12.8°, respectively. The similar wettability means that the surface properties of ETLs will have a minimal impact on the crystallization of PbI_2. Additionally, in Figure S5, the SnO_2 nanoparticles show good dispersibility, thereby indicating that a small amount of CA does not induce the aggregation of SnO_2.

In this work, a two-step sequential deposition process was employed to fabricate the perovskite film because of its high film quality, which is essential for the fabrication of high-efficiency and reproducible PSCs.[34−36] We first investigated the changes in microscale morphology of the as-prepared PbI_2 and perovskite films near the ETL, which were peeled off using a mechanical method according to a published report.[37] Both cross-sectional images of PbI_2 thin films are shown in Figure 1c,e. For the control sample, the PbI_2 film has coralloid crystalline grains with a mesoporous structure, while the target PbI_2 film shows a more densely packed structure. We peeled off the PbI_2 films in the direction indicated by the right angle arrows near the ETL substrates. The corresponding SEM images of the bottom surface of the PbI_2 films are shown in Figure 1d,f. In comparison with the control PbI_2, the target PbI_2 film appears to have a more condensed structure with a distinctly fibrous feature. The changes in micromorphologies can be attributed to the chemical interaction between organic acid and PbI_2, which indicates the organic acid molecules play a critical role to the crystallization of PbI_2 instead of other factors, such as wettability or solvents.[38,39] The grazing incidence X-ray diffraction (GIXRD) technique was used to investigate the crystalline properties of PbI_2 films on the bottom side. The incident angle was set at 0.5° for the measurement with a penetration depth of ∼300 nm,[40] as shown in Figure 1g. The (001) diffraction peak at 12.8° for the target PbI_2 films is higher compared with the control film, which suggests the enhanced crystallinity of PbI_2. We prepared the perovskite using the as-deposited PbI_2 films and checked for the cross-sectional images of perovskite films, as presented in Figure 1h,i. Additionally, the top surface morphologies of the perovskite films are displayed in Figure S6. Compared with the control film, the target perovskite film possesses a more compact and uniform film quality with fewer grain boundaries. Figure 1j,k shows the bottom surfaces of peeled perovskite films on different ETLs. It is noticed that there are some white clusters present in the control perovskite film, which can be

https://doi.org/10.1021/acsenergylett.4c00386
ACS Energy Lett. 2024, 9, 2659−2669

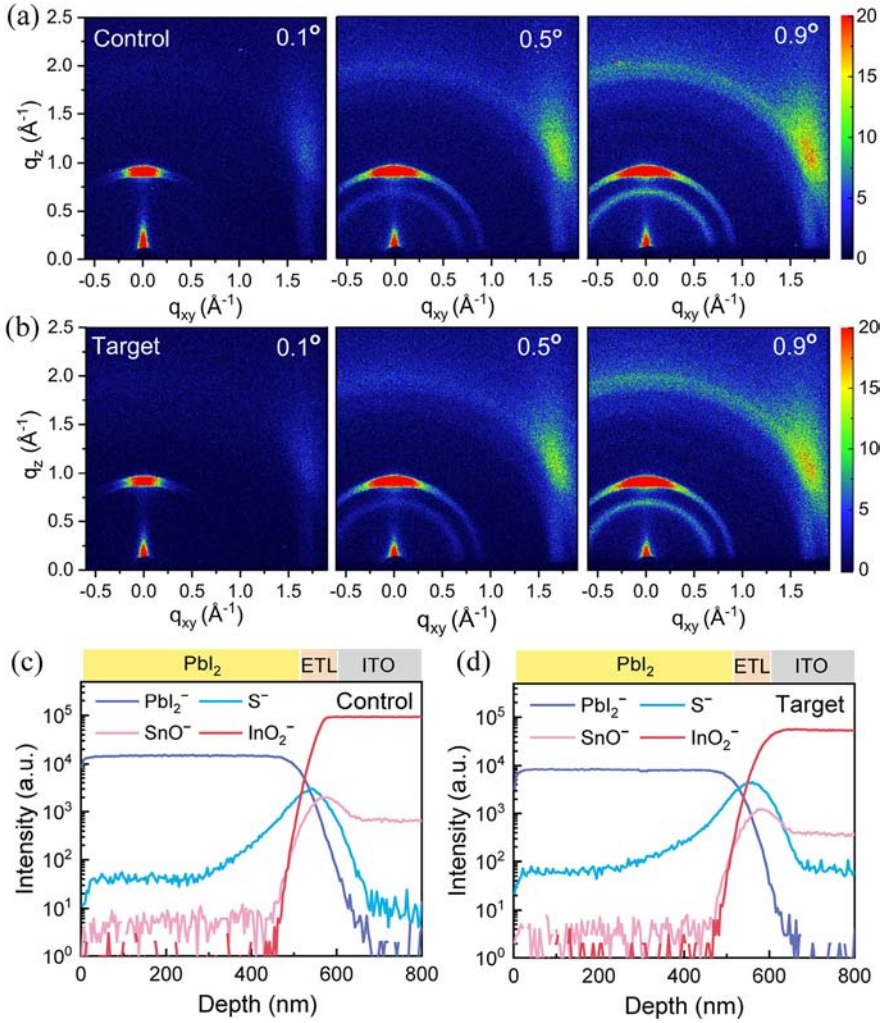

Figure 3. Crystallographic and depth characterization of the PbI_2 films. (a,b) 2D GIWAXS patterns with different incident angles of as-prepared PbI_2 films (70 °C, 60 s). (c,d) ToF-SIMS depth profiles of as-prepared PbI_2 films (70 °C, 60 s).

identified to be residual PbI_2.[19,41] However, these PbI_2 clusters are completely absent at the bottom surface of the target perovskite film, as observed from SEM images. Besides, we investigated the X-ray diffraction spectra (XRD) of the whole perovskite films deposited on various ETLs, as shown in Figure 1l. The area ratio of the PbI_2 peak decreased from 67% to 35% after being subjected to CA treatment, which can be ascribed to the reduction in the amount of PbI_2 present at the buried interface.

We performed the scanning transmission election microscope (STEM) to investigate the atomistic configuration change of PbI_2 nearby ETL. The PbI_2 slices were achieved using focused ion beam (FIB), and the corresponding cross-sectional STEM images are shown in Figure 2. In Figure 2a, the control PbI_2 film exhibits stratification with the top layer consisting of crystalline grains that are clearly visible and well defined. However, the bottom layer shows a dark region that lacks any crystalline structure, thereby indicating its amorphous nature. Upon closer examination of the amorphous region near the ETL, two small PbI_2 grains are observed (regions 1 and 2). These grains, comparatively small, provide evidence of the poor crystallization of PbI_2 on the bottom side. In Figure 2b,c, we analyze the atomic STEM images and corresponding fast Fourier transform (FFT) patterns of these grains. It was found that the control PbI_2 grains exhibited crystal planes of $(\bar{1}10)$ and (001) with interplane distances of 2.33 and 7.25 Å along the $[1\bar{1}0]$ and $[\bar{1}10]$ zone axis, respectively. Furthermore, two additional neighboring regions were investigated and are shown in Figure S7. Both regions show lower crystallinity levels and ultrasmall grain size, which is a common issue found in the control PbI_2 film. In Figure 2d, orientated growth with a fibrous crystal structure is observed for the target PbI_2 film, which is consistent with the observation in the SEM images. Unlike the control sample, the target PbI_2 film exhibited larger crystal grains, which indicates enhanced crystallinity. In Figure 2e,f, the Pb−I arrangements in regions 3 and 4 were analyzed, and the corresponding interplanar distances were calculated to be 5.76 and 7.22 Å, which are indicative of the (001) crystal plane of PbI_2. In Figure S8, six additional neighboring regions were chosen, and all of them have large PbI_2 grains, which indicates a high degree of the crystallinity and uniformity in the target PbI_2 film near the ETL. We calculated the adsorption energies of $(\bar{1}10)$ and (001) crystal planes with FA^+ cation to show the chemical interaction mechanism for the formation of perovskite. The optimized molecular structures of the $(\bar{1}10)$ and (001) crystal planes with FA^+ cation are shown in Figure S9. It shows that the adsorption energy of FA^+ cation on the (001)

https://doi.org/10.1021/acsenergylett.4c00386
ACS Energy Lett. 2024, 9, 2659−2669

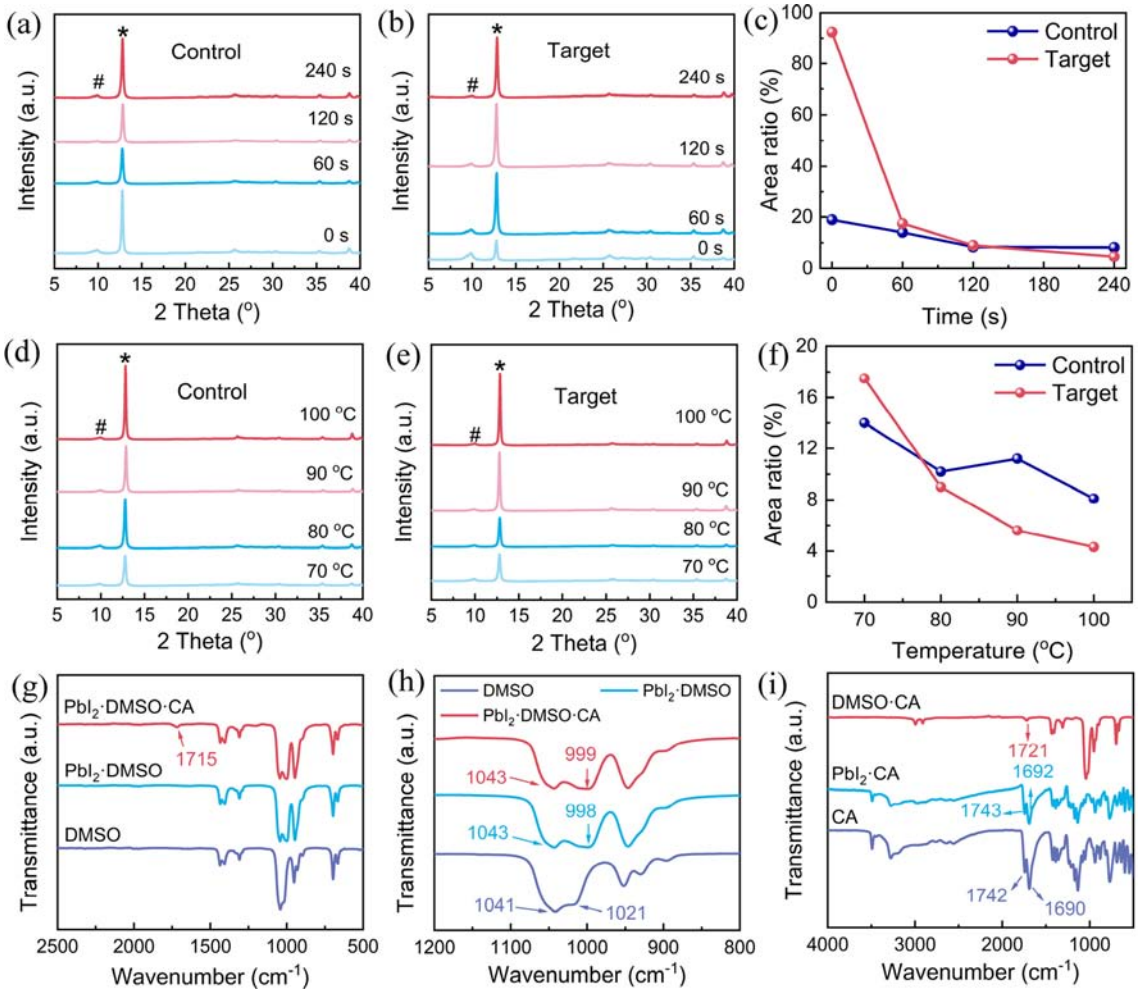

Figure 4. Crystallization process and chemical interaction between PbI_2DMSO and CA. (a,b) XRD patterns of PbI_2 precursor films annealed at 70 °C with varying annealing times. (c) Area ratio variation of PbI_2DMSO (#) and PbI_2 (*) diffraction peaks over time. (d,e) XRD patterns of PbI_2 precursor films annealed at different temperatures for 60 s. (f) Area ratio variation of PbI_2DMSO (#) and PbI_2 (*) diffraction peaks over temperature. (g,h) FTIR spectra of DMSO, PbI_2DMSO, and PbI_2DMSO·CA solutions. (i) FTIR spectra of CA (powder), PbI_2CA (grinded powder), and DMSO·CA (liquid).

crystal plane is −0.94 eV, which is larger than that of the $(\overline{1}10)$ plane (−0.63 eV), thereby meaning that the (001) plane can easily react with FA^+ cations to form perovskite by consuming PbI_2 at the bottom surface.

To gain a comprehensive understanding of the crystallographic characterization of the as-prepared PbI_2 films, grazing incidence wide-angle X-ray scattering (GIWAXS) was performed with various incident angles, which can be seen in Figure 3a,b. By changing the incident angle from 0.1° to 0.9°, the estimated penetration depth of X-ray beam ranges from 3 to 500 nm.[42] The diffraction at $q \approx 0.9$ Å^{-1} relates to the (001) plane of the PbI_2 film. Additionally, a weak diffraction ring that can be seen at $q \approx 0.7$ Å^{-1} with an incident angle of 0.5° relates to the PbI_2·DMSO complex, which is randomly oriented inside the film. Because of the low annealing temperature of 70 °C, the PbI_2·DMSO complex can be observed in both samples. As the incident angle increases, the halo gradually brightens, thereby indicating that the PbI_2·DMSO complex is primarily located inside the PbI_2 film rather than on the surface. Time-of-flight secondary ion mass spectrometry (ToF-SIMS) was also performed to show the depth distribution of the PbI_2·DMSO intermediate phase. As shown in Figure 3c,d, the dominant peak of S^- relating to the DMSO-based intermediate phase mainly distributes near the ETL substrate, which is consistent with the GIWAXS result.

To better understand the crystallization process of PbI_2, we conducted XRD to characterize the as-prepared PbI_2 films. The XRD spectra of PbI_2 films annealed at 70 °C with different annealing times are displayed in Figure 4a,b. The diffraction peaks at 9.9° and 12.8° relate to the PbI_2·DMSO complex and (001) plane of PbI_2, respectively.[43−45] We analyzed the change in the area ratio of the diffraction peak of $(PbI_2$·DMSO$)/PbI_2$ with respect to the annealing time, which is shown in Figure 4c and Table S1. At 0 s, the area ratio for the target PbI_2 precursor film was found to be significantly higher, reaching 92.3%, which can be ascribed to the decline of the PbI_2 diffraction peak displayed in Figure S10. For the control PbI_2 film, the area ratio decreased to 18.9%. After annealing at 70 °C for 60 s, the area ratios for both cases presented a considerable level, consistent with the results of GIWAXS. As the annealing time increased, the area ratio for the control sample remained relatively constant with only a slight decrease from 8.4% to 8.2% between annealing times of 120 and 240 s. In the case of the target sample, the area ratio dropped from 9% at 120 s to 4.7% at 240 s, which indicates the decomposition of PbI_2·DMSO. We also compared the XRD spectra of as-prepared

https://doi.org/10.1021/acsenergylett.4c00386
ACS Energy Lett. 2024, 9, 2659−2669

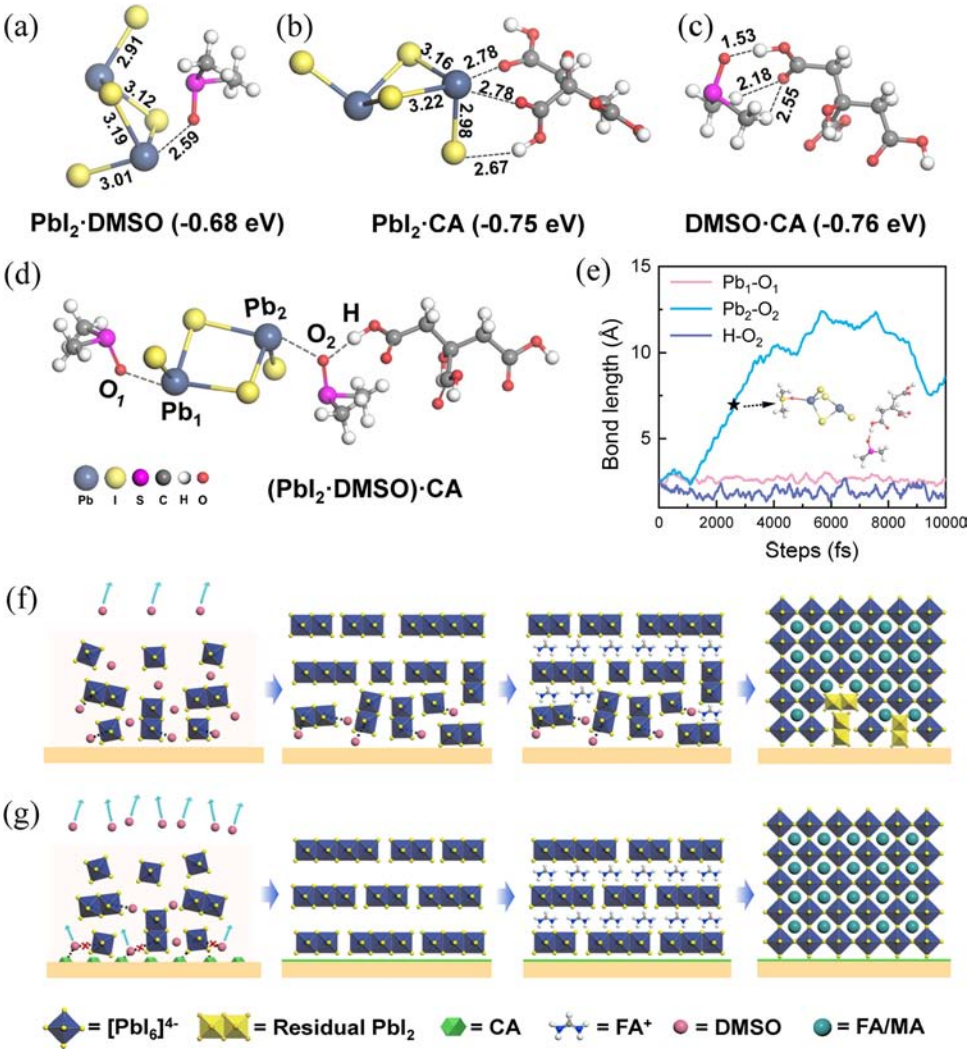

Figure 5. Molecular dynamics and growth mechanism of perovskite. (a−d) Schematic diagram of the molecular interaction of PbI_2·DMSO, PbI_2·CA, DMSO·CA, and (PbI_2·DMSO)·CA. (e) Bond length change of (PbI_2·DMSO)·CA at an accelerated temperature of 127°C (400 K). (f) Control and (g) target perovskite growth mechanism to illustrate the elimination of residual PbI_2.

PbI_2 films annealed at various temperatures for 60 s, which are depicted in Figure 4d,f and Table S2. At a low temperature of 70 °C, the amount of PbI_2·DMSO for the target sample was marginally higher than that of the control sample, but it suffers a much faster decline compared with the latter. As the temperature increased to 100 °C, the area ratio for target PbI_2 film decreased to 4.3%, while it was 8.1% for control PbI_2. The rapid decrease of area ratio for the target film again confirms the fast decomposition of PbI_2·DMSO under thermal annealing. Additionally, the PbI_2·DMSO peak completely disappeared after annealing at 150 °C for 10 min, as shown in Figure S11. On the basis of the above results, it can be inferred that the organic acid molecules can remove the PbI_2·DMSO complex and enhance the crystallinity of PbI_2 at the bottom side.

FTIR was performed to analyze the chemical interaction between CA and PbI_2·DMSO complex, as illustrated in Figure 4g−i. In Figure 4g, a new peak emerged at 1715 cm^{-1} for PbI_2·DMSO·CA corresponding to the vibration of −COOH group, which is lower than the 1742 cm^{-1} observed for CA powder (Figure S2) because of the formation of a hydrogen bond, thereby confirming the interaction between CA and PbI_2·DMSO. Magnifying the FTIR spectra in Figure 4h, two peaks at 1042 and 1021 cm^{-1} of DMSO solution can be assigned to the vibration stretching of free and hydrogen-bonded S═O bonds.[46] However, the shoulder peak at 1021 cm^{-1} is shifted to 998 cm^{-1} for PbI_2·DMSO and 999 cm^{-1} for PbI_2·DMSO·CA, respectively. These shifts can be attributed to the increased electron cloud density near the oxygen atom after interacting with a less electronegative lead atom.[47] In addition, a slightly higher wavenumber is observed after incorporating CA because of the formation of the Pb−O−H bond. In Figure 4i, the stretching vibration of C═O of CA that situates at 1690 cm^{-1} is shifted to a higher wavenumber of 1692 cm^{-1} for grinded PbI_2·CA powder because of the donation of an electron pair from CA to Pb^{2+}. In DMSO·CA solution, the C═O vibration is shifted to 1721 cm^{-1} because of the formation of hydrogen bonds between the CA molecule and its surroundings. Given the rapid decomposition of PbI_2·DMSO and the chemical interaction among the three, we deduce that CA and DMSO interact with PbI_2 through a strong competitive adsorption effect, which ultimately affects the crystallization process of PbI_2.

We performed theoretical calculations to study the interactions among CA, PbI_2, and DMSO, as shown in Figure 5. The optimized molecular structures of PbI_2·DMSO, PbI_2·

https://doi.org/10.1021/acsenergylett.4c00386
ACS Energy Lett. 2024, 9, 2659−2669

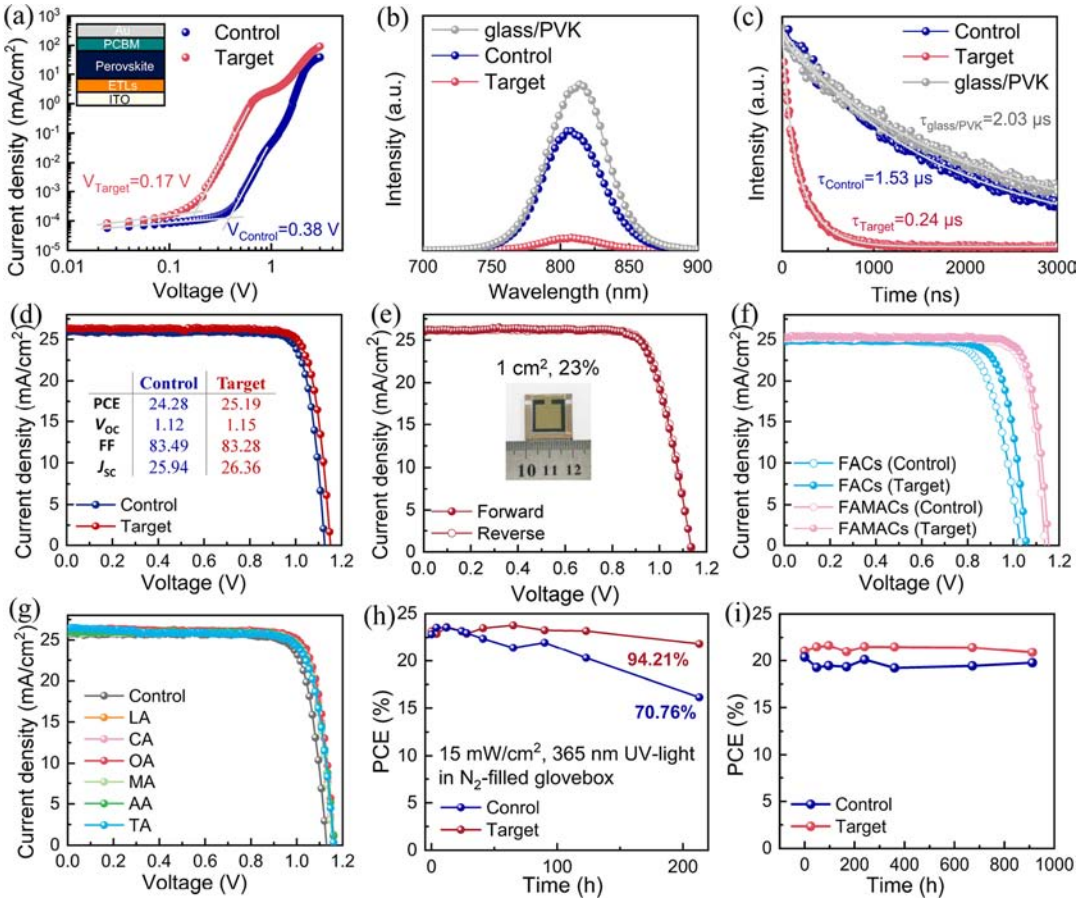

Figure 6. Charge carrier dynamics and photovoltaic performance of perovskite solar cells. (a) Dark *J*−*V* curves of semidevices with an architecture of ITO/ETL/perovskite/PCBM/Au. (b) SSPL spectra and (c) TRPL spectra of perovskite films deposited on different substrates. (d) *J*−*V* curves of best performing PSCs using FAMA-based perovskites with an aperture area of 0.1 cm^2. (e) *J*−*V* curves of a 1 cm^2 PSC with forward and reverse scan. (f) *J*−*V* curves of PSCs using FACs- or FAMACs-based perovskites. (g) *J*−*V* curves of PSCs based on different organic acids capped SnO_2 ETLs. (h) Light stability of the PSCs measured with a 365 nm UV lamp (15 mW/cm^2). (i) Air stability of the PSCs stored in air with a humidity of 15 ± 5%.

CA, and DMSO·CA are plotted in Figure 5a−c, and the corresponding binding energies were calculated to be −0.68, −0.75, and −0.76 eV, respectively, which confirms the chemical interaction observed from the FTIR results. We observed a slightly higher binding energy of PbI_2·CA compared with that of PbI_2·DMSO, which indicates that the PbI_2 molecule prefers to interact with CA rather than DMSO. Furthermore, we noted that CA and DMSO also exhibit a high binding energy of −0.76 eV, which indicates a strong intermolecular interaction through hydrogen bonds. *Ab initio* molecular dynamics simulation has been performed to get a deep insight of the molecular dynamics of CA and PbI_2·DMSO, as shown in Figure 5d, Video S1, and Video S2. When we monitored the bond length change of Pb_1-O_1, Pb_2-O_2, and $H-O_2$ at an accelerated temperature of 127 °C (400 K), we observed that the bond length change for Pb_1-O_1 and $H-O_2$ varied within a reasonable range. However, a sharp bond length increase was observed for Pb_2-O_2, which suggests the decomposition of PbI_2·DMSO. As can be seen from Video S1, CA molecule drags the nearby DMSO away from PbI_2 through hydrogen bond interaction. It is worth noting that this process will not occur at a low temperature of 27 °C (300 K), as shown in Figure S12 and Video S2. We proposed a credible mechanism to elucidate the influence of the CA molecule on the crystallization process of perovskite films, as shown in Figure 5f,g. In Figure 5f, after deposition of the PbI_2 precursor, excess DMSO at the bottom side cannot easily escape because of the strong chemical interaction with PbI_2, which prohibits amine salts from entering the amorphous PbI_2 framework. This results in the formation of PbI_2 residuals at the bottom surface of the perovskite, as seen in Figure 1j. In contrast, when the PbI_2 precursor was deposited on the target substrate, CA molecules broke the S═O−Pb bond and accelerated the decomposition of PbI_2·DMSO by forming (001)-oriented crystal grains. The high crystallinity is beneficial for the diffusion of amines toward the bottom of the substrate and promoting the formation of perovskite, which results in the elimination of the excess PbI_2 observed in the SEM images and XRD patterns.

The space-charge-limited current (SCLC) method is a widely used technique for characterizing the presence of defects within the crystal structure.[48,49] Semidevices with an architecture of ITO/SnO_2/perovskite/PCBM/Au were prepared and measured under dark condition. The logarithmic *I*−*V* curves of semidevices are shown in Figure 6a. The V_{TFL}s of semidevices were calculated to be 0.38 and 0.17 V for the control and the target devices, respectively. The trap density (N_{trap}) of the perovskite films is calculated according to the formula $N_{trap} = 2\varepsilon_0\varepsilon_r V_{TFL}/qL^2$, where ε_0 and ε_r are the vacuum dielectric constant and relative dielectric constant, and q and L

https://doi.org/10.1021/acsenergylett.4c00386
ACS Energy Lett. 2024, 9, 2659−2669

stand for the elementary charge (1.6×10^{-19} C) and thickness of the perovskite (800 nm), respectively. N_{trap} was calculated to be 1.38×10^{15} cm^{-3} for the control device, whereas it decreased to 0.5×10^{15} cm^{-3} for the target device. This indicates that the trap defects were effectively reduced with a suppressed nonradiative recombination. Steady-state photoluminescence (SSPL) and time-resolved photoluminescence (TRPL) spectra were performed to study the charge carrier dynamics at the ETL/perovskite interface, as shown in Figure 6b,c. The direction of the incident light is from the ETL layer to the perovskite film. The SSPL intensity of the perovskite film deposited on the target substrate was found to be much lower than the control one, which indicates that the charge carriers were effectively transported from perovskite to target ETL. The charge carrier lifetime is calculated by fitting the TRPL spectra in Figure 6c. For the perovskite deposited on the bare glass substrate, the average lifetime was 2.03 μs, while it decreased to 1.53 μs for the control device and 0.24 μs for the target one. The decreased lifetime for the latter indicates a fast charge carrier transport from perovskite to ETL, which can be ascribed to the reduced trap defects and improved interface contact.

We fabricated devices and checked the photovoltaic performance of the PSCs with different ETLs using a formamidinium methylammonium (FAMA)-based perovskite. Statistical efficiency of devices using different ETLs was summarized in Figure S13. The average PCE increased from 23.96% to 24.82%, the average current density (J_{SC}) increased from 25.93 to 26.19 mA/cm^2, the open-circuit voltage (V_{OC}) rose from 1.13 to 1.15 V, and the fill factor (FF) increased from 82.04% to 82.46%, respectively. Both control and target PSCs exhibit negligible hysteresis, as shown in Figure S14. In Figure 6d, the efficiency of PSC was improved from 24.28% for the control device to 25.19% for the target device, which was mainly ascribed to the increase of J_{SC} from 25.94 to 26.36 mA/cm^2 and V_{OC} from 1.12 to 1.15 V. We also prepared a 1 cm^2 large-area device and achieved an efficiency of 23% without hysteresis, as shown in Figure 6e. The improvement in J_{SC} and V_{OC} can be ascribed to the improved interfacial contact and reduced PbI_2 defects at the bottom surface. Besides, a certified efficiency of 24.64% was achieved under a humidity of 50% for the target PSC without encapsulation, as shown in Figure S15. Figure S16 shows the external quantum efficiency (EQE) curves of the PSCs on the basis of different ETLs. A slightly higher light absorption was observed for the target PSC compared with the control PSC, with integrated J_{SC} increased from 24.9 to 25.16 mA/cm^2. We explored the effectiveness of various amine cations using the target ETL to demonstrate the universality of this strategy, including formamidinium cesium (FACs) and formamidinium methylammonium cesium (FAMACs) cations, as shown in Figure 6f and Table S3. Remarkably, all of the PSCs that were fabricated using the target ETL demonstrated enhanced efficiency, irrespective of the specific amine cations employed. We also prepared PSCs using different organic acids, as mentioned above. As shown in Figure 6g and Table S4, the efficiencies of PSCs utilizing various organic acids were found to be comparable with that of the CA-based device. What's more, all the PSCs based on organic acids demonstrate higher efficiencies than the control PSC, thereby highlighting the significant potential of organic acids in manipulating the buried interface and enhancing the performance of the PSCs.

The stability of the PSCs was monitored and is shown in Figure 6h,i. In Figure 6h, the light stability of the PSCs was carried out under a 15 mW/cm^2 ultraviolet (UV) source with a wavelength of 365 nm. The target device demonstrates an enhanced stability and maintains 94.21% of its initial efficiency, while only 70.76% of the initial efficiency is maintained for the control PSC. In addition, the maximum power point (MPP) tracking of unencapsulated PSC was also conducted under 1 sun illumination in air with a relative humidity of ~40%, as shown in Figure S17, which showed improved operando stability. The air stability of the PSCs was also assessed, as shown in Figure 6i, where the PSCs were stored in a drybox with a relative humidity of 15 ± 5%. Both types of PSCs demonstrated a negligible decline after 900 h, thereby indicating good air stability. These results indicate that the quality of the buried interface holds greater significance in improving light stability.

Residual PbI_2 at the buried interface significantly influences the efficiency and stability of the PSCs. In this work, we showed that the formation of residual PbI_2 at the buried interface was related to the decomposition of the PbI_2·DMSO complex. It was proved that the chemical bond of PbI_2·DMSO could be broken by CA, thereby facilitating the crystallization of PbI_2, which led to the intercalation of amine cations into PbI_2 octahedron cages by forming stable perovskite. The reduced residual PbI_2 at the bottom surface of the perovskite improved the interfacial contact between ETL and perovskite with reduced nonradiative recombination. As a result, the efficiency of the PSC was improved to 25.19% for the target PSC with a certified efficiency of 24.64% and a 1 cm^2 PSC of 23%. The target PSC also demonstrates good UV light stability by retaining 94.21% of its initial efficiency after 200 h of UV light soaking. This work provides a profound strategy for efficiently manipulating the residual PbI_2 at the bottom surface of perovskite through the molecular interaction mechanism, which holds immense potential for the development of high-performance PSCs with good stability.

■ ASSOCIATED CONTENT

Supporting Information

The Supporting Information is available free of charge at https://pubs.acs.org/doi/10.1021/acsenergylett.4c00386.

Experimental section including materials, device fabrication, characterization, and calculation; molecular structure of organic acids; FTIR, contact angles, and TEM characterization of ETLs; morphologies of PbI_2 and perovskite films; XRD analysis of PbI_2; and $I-V$ statistics, $J-V$ hysteresis, EQE, corresponding $J-V$ parameters, efficiency certification details, and MPP tracking of PSCs (PDF)

Ab initio molecular dynamics simulation of molecular dynamics of (PbI_2·DMSO)·CA at 400 K (MP4)

Ab initio molecular dynamics simulation of molecular dynamics of (PbI_2·DMSO)·CA at 300 K (MP4)

■ AUTHOR INFORMATION

Corresponding Authors

Meicheng Li − *State Key Laboratory of Alternate Electrical Power System with Renewable Energy Sources, School of New Energy, North China Electric Power University, Beijing 102206, China;* orcid.org/0000-0002-0731-741X; Email: mcli@ncepu.edu.cn

https://doi.org/10.1021/acsenergylett.4c00386
ACS Energy Lett. 2024, 9, 2659−2669

Nam-Gyu Park − *School of Chemical Engineering, SKKU Institute of Energy Science and Technology (SIEST), Sungkyunkwan University, Suwon 16419, Korea;* orcid.org/0000-0003-2368-6300; Email: npark@skku.edu

Authors

Xing Zhao − *State Key Laboratory of Alternate Electrical Power System with Renewable Energy Sources, School of New Energy, North China Electric Power University, Beijing 102206, China;* orcid.org/0000-0002-3323-2014

Yujie Qiu − *State Key Laboratory of Alternate Electrical Power System with Renewable Energy Sources, School of New Energy, North China Electric Power University, Beijing 102206, China*

Min Wang − *State Key Laboratory of Alternate Electrical Power System with Renewable Energy Sources, School of New Energy, North China Electric Power University, Beijing 102206, China*

Danxia Wu − *State Key Laboratory of Alternate Electrical Power System with Renewable Energy Sources, School of New Energy, North China Electric Power University, Beijing 102206, China*

Xiaopeng Yue − *State Key Laboratory of Alternate Electrical Power System with Renewable Energy Sources, School of New Energy, North China Electric Power University, Beijing 102206, China*

Huilin Yan − *State Key Laboratory of Alternate Electrical Power System with Renewable Energy Sources, School of New Energy, North China Electric Power University, Beijing 102206, China*

Bingbing Fan − *State Key Laboratory of Alternate Electrical Power System with Renewable Energy Sources, School of New Energy, North China Electric Power University, Beijing 102206, China*

Shuxian Du − *State Key Laboratory of Alternate Electrical Power System with Renewable Energy Sources, School of New Energy, North China Electric Power University, Beijing 102206, China*

Yuqing Yang − *State Key Laboratory of Alternate Electrical Power System with Renewable Energy Sources, School of New Energy, North China Electric Power University, Beijing 102206, China*

Yingying Yang − *State Key Laboratory of Alternate Electrical Power System with Renewable Energy Sources, School of New Energy, North China Electric Power University, Beijing 102206, China*

Danni Li − *State Key Laboratory of Alternate Electrical Power System with Renewable Energy Sources, School of New Energy, North China Electric Power University, Beijing 102206, China*

Peng Cui − *State Key Laboratory of Alternate Electrical Power System with Renewable Energy Sources, School of New Energy, North China Electric Power University, Beijing 102206, China*

Hao Huang − *State Key Laboratory of Alternate Electrical Power System with Renewable Energy Sources, School of New Energy, North China Electric Power University, Beijing 102206, China*

Yingfeng Li − *State Key Laboratory of Alternate Electrical Power System with Renewable Energy Sources, School of New Energy, North China Electric Power University, Beijing 102206, China*

Complete contact information is available at: https://pubs.acs.org/10.1021/acsenergylett.4c00386

Author Contributions

X.Z. designed the experiment and wrote the manuscript. M.L. supervised the work. N.-G.P. revised the manuscript. Y.Q. assisted with the STEM characterization and analysis. M.W. performed the calculation section of the study. D.W. and X.Y. conducted part of the experimental work. H.Y. helped conduct the air-stability measurements. S.D. helped perform the light-stability test of the PSCs. B.F., Yuqing Y., Yingying Y., D.L., P.C., H.H., and Y.L. took part in the experimental discussion and revised the manuscript.

Notes

The authors declare no competing financial interest.

■ ACKNOWLEDGMENTS

This work is supported partially by the Key Research and Development Program sponsored by the Ministry of Science and Technology (MOST) (Grant no. 2022YFB4200301); National Natural Science Foundation of China (Grant nos. 52232008, 51972110, 52102245, and 52072121); Beijing Natural Science Foundation (2222076 and 2222077); Beijing Nova Program (20220484016); Young Elite Scientists Sponsorship Program by CAST (2022QNRC001); 2022 Strategic Research Key Project of Science and Technology Commission of the Ministry of Education, Huaneng Group Headquarters Science and Technology Project (HNKJ20-H88); the Fundamental Research Funds for the Central Universities (2022MS029, 2022MS02, 2022MS031, 2023MS042, and 2023MS047); and the NCEPU "Double First-Class" Program. N.-G.P. acknowledges the financial support from the National Research Foundation of Korea (NRF) grants funded by the Korean government (MSIT) under contract NRF-2021R1A3B1076723 (Research Leader Program).

■ REFERENCES

(1) Kim, H.-S.; Lee, C.-R.; Im, J.-H.; Lee, K.-B.; Moehl, T.; Marchioro, A.; Moon, S.-J.; Humphry-Baker, R.; Yum, J.-H.; Moser, J. E.; Grätzel, M.; Park, N.-G. Lead Iodide Perovskite Sensitized All-Solid-State Submicron Thin Film Mesoscopic Solar Cell with Efficiency Exceeding 9%. *Sci. Rep.* **2012**, *2*, 591.

(2) Lee, J. W.; Kim, D. H.; Kim, H. S.; Seo, S. W.; Cho, S. M.; Park, N. G. Formamidinium and Cesium Hybridization for Photo- and Moisture-Stable Perovskite Solar Cell. *Adv. Energy Mater.* **2015**, *5* (20), 1501310.

(3) Yan, L.; Huang, H.; Cui, P.; Du, S.; Lan, Z.; Yang, Y.; Qu, S.; Wang, X.; Zhang, Q.; Liu, B.; Yue, X.; Zhao, X.; Li, Y.; Li, H.; Ji, J.; Li, M. Fabrication of Perovskite Solar Cells in Ambient Air by Blocking Perovskite Hydration with Guanabenz Acetate Salt. *Nat. Energy* **2023**, *8* (10), 1158−1167.

(4) Jeon, N. J.; Noh, J. H.; Yang, W. S.; Kim, Y. C.; Ryu, S.; Seo, J.; Seok, S., Il Compositional Engineering of Perovskite Materials for High-Performance Solar Cells. *Nature* **2015**, *517* (7535), 476−480.

(5) Cui, P.; Qu, S.; Zhang, Q.; Liu, B.; Yan, L.; Du, S.; Wang, X.; Huang, H.; Ji, J.; Li, M. Homojunction Perovskite Solar Cells: Opportunities and Challenges. *Energy Mater.* **2022**, *1* (2), 100014.

(6) Jeon, N. J.; Noh, J. H.; Kim, Y. C.; Yang, W. S.; Ryu, S.; Seok, S., Il Solvent Engineering for High-Performance Inorganic-Organic Hybrid Perovskite Solar Cells. *Nat. Mater.* **2014**, *13*, 897−903.

(7) Rezaee, E.; Zhang, W.; Silva, S. R. P. Solvent Engineering as a Vehicle for High Quality Thin Films of Perovskites and Their Device Fabrication. *Small* **2021**, *17* (25), 20081415.

(8) Wang, S.; Li, M.-H.; Jiang, Y.; Hu, J.-S. Instability of Solution-Processed Perovskite Films: Origin and Mitigation Strategies. *Mater. Futur.* **2023**, *2* (1), 012102.
(9) Wei, D.; Ma, F.; Wang, R.; Dou, S.; Cui, P.; Huang, H.; Ji, J.; Jia, E.; Jia, X.; Sajid, S.; Elseman, A. M.; Chu, L.; Li, Y.; Jiang, B.; Qiao, J.; Yuan, Y.; Li, M. Ion-Migration Inhibition by the Cation-π Interaction in Perovskite Materials for Efficient and Stable Perovskite Solar Cells. *Adv. Mater.* **2018**, *30* (31), 1707583.
(10) Zhou, H.; Chen, Q.; Li, G.; Luo, S.; Song, T.; Duan, H.-S.; Hong, Z.; You, J.; Liu, Y.; Yang, Y. Interface Engineering of Highly Efficient Perovskite Solar Cells. *Science.* **2014**, *345* (6196), 542−547.
(11) Huang, H.; Cui, P.; Chen, Y.; Yan, L.; Yue, X.; Qu, S.; Wang, X.; Du, S.; Liu, B.; Zhang, Q.; Lan, Z.; Yang, Y.; Ji, J.; Zhao, X.; Li, Y.; Wang, X.; Ding, X.; Li, M. 24.8%-Efficient Planar Perovskite Solar Cells via Ligand-Engineered TiO_2 Deposition. *Joule* **2022**, *6* (9), 2186−2202.
(12) Fu, G.; Lee, D. K.; Ma, C.; Park, N. G. Disulfidation Interfacial Engineering toward Stable, Lead-Immobilizable Perovskite Solar Cells. *ACS Energy Lett.* **2023**, *8* (11), 4563−4571.
(13) National Renewable Energy Laboratory. *Best Research-Cell Efficiency Chart.* https://www.nrel.gov/pv/cell-efficiency.html (accessed 2024-01-31).
(14) Chen, B.; Rudd, P. N.; Yang, S.; Yuan, Y.; Huang, J. Imperfections and Their Passivation in Halide Perovskite Solar Cells. *Chem. Soc. Rev.* **2019**, *48* (14), 3842−3867.
(15) Lim, E. L.; Wei, Z. A Short Overview of the Lead Iodide Residue Impact and Regulation Strategies in Perovskite Solar Cells. *J. Energy Chem.* **2024**, *90*, 504−510.
(16) Chen, Q.; Zhou, H.; Song, T.-B.; Luo, S.; Hong, Z.; Duan, H. S.; Dou, L.; Liu, Y.; Yang, Y. Controllable Self-Induced Passivation of Hybrid Lead Iodide Perovskites toward High Performance Solar Cells. *Nano Lett.* **2014**, *14* (7), 4158−4163.
(17) Liu, F.; Dong, Q.; Wong, M. K.; Djurišić, A. B.; Ng, A.; Ren, Z.; Shen, Q.; Surya, C.; Chan, W. K.; Wang, J.; Ng, A. M. C.; Liao, C.; Li, H.; Shih, K.; Wei, C.; Su, H.; Dai, J. Is Excess PbI_2 Beneficial for Perovskite Solar Cell Performance? *Adv. Energy Mater.* **2016**, *6* (7), 1502206.
(18) Liang, J.; Hu, X.; Wang, C.; Liang, C.; Chen, C.; Xiao, M.; Li, J.; Tao, C.; Xing, G.; Yu, R.; Ke, W.; Fang, G. Origins and Influences of Metallic Lead in Perovskite Solar Cells. *Joule* **2022**, *6* (4), 816−833.
(19) Yang, X.; Luo, D.; Xiang, Y.; Zhao, L.; Anaya, M.; Shen, Y.; Wu, J.; Yang, W.; Chiang, Y. H.; Tu, Y.; Su, R.; Hu, Q.; Yu, H.; Shao, G.; Huang, W.; Russell, T. P.; Gong, Q.; Stranks, S. D.; Zhang, W.; Zhu, R. Buried Interfaces in Halide Perovskite Photovoltaics. *Adv. Mater.* **2021**, *33* (7), 2006435.
(20) Wang, X.; Huang, H.; Wang, M.; Lan, Z.; Cui, P.; Du, S.; Yang, Y.; Yan, L.; Zhang, Q.; Qu, S.; Li, M. Oriented Molecular Bridge Constructs Homogeneous Buried Interface for Perovskite Solar Cells with Efficiency Over 25.3%. *Adv. Mater.* **2024**, 2310710.
(21) Zhuang, Q.; Zhang, C.; Gong, C.; Li, H.; Li, H.; Zhang, Z.; Yang, H.; Chen, J.; Zang, Z. Tailoring Multifunctional Anion Modifiers to Modulate Interfacial Chemical Interactions for Efficient and Stable Perovskite Solar Cells. *Nano Energy* **2022**, *102*, 107747.
(22) Dong, Q.; Zhu, C.; Chen, M.; Jiang, C.; Guo, J.; Feng, Y.; Dai, Z.; Yadavalli, S. K.; Hu, M.; Cao, X.; Li, Y.; Huang, Y.; Liu, Z.; Shi, Y.; Wang, L.; Padture, N. P.; Zhou, Y. Interpenetrating Interfaces for Efficient Perovskite Solar Cells with High Operational Stability and Mechanical Robustness. *Nat. Commun.* **2021**, *12*, 973.
(23) Gao, Y.; Ren, F.; Sun, D.; Li, S.; Zheng, G.; Wang, J.; Raza, H.; Chen, R.; Wang, H.; Liu, S.; Yu, P.; Meng, X.; He, J.; Zhou, J.; Hu, X.; Zhang, Z.; Qiu, L.; Chen, W.; Liu, Z. Elimination of Unstable Residual Lead Iodide near the Buried Interface for the Stability Improvement of Perovskite Solar Cells. *Energy Environ. Sci.* **2023**, *16* (5), 2295−2303.
(24) Qin, Z.; Chen, Y.; Wang, X.; Wei, N.; Liu, X.; Chen, H.; Miao, Y.; Zhao, Y. Zwitterion-Functionalized SnO_2 Substrate Induced Sequential Deposition of Black-Phase $FAPbI_3$ with Rearranged PbI_2 Residue. *Adv. Mater.* **2022**, *34* (32), 2203143.
(25) Wu, M.; Duan, Y.; Yang, L.; You, P.; Li, Z.; Wang, J.; Zhou, H.; Yang, S.; Xu, D.; Zou, H.; Liu, Z. Multifunctional Small Molecule as Buried Interface Passivator for Efficient Planar Perovskite Solar Cells. *Adv. Funct. Mater.* **2023**, *33* (22), 2300128.
(26) Liu, B.; Zhou, Q.; Li, Y.; Chen, Y.; He, D.; Ma, D.; Han, X.; Li, R.; Yang, K.; Yang, Y.; Lu, S.; Ren, X.; Zhang, Z.; Ding, L.; Feng, J.; Yi, J.; Chen, J. Polydentate Ligand Reinforced Chelating to Stabilize Buried Interface toward High-Performance Perovskite Solar Cells. *Angew. Chemie Int. Ed.* **2024**, *63* (8), No. e202317185.
(27) Zhuang, X.; Ma, D.; Li, G.; Yang, Z.; Zhang, Z.; Zhao, J.; Chi, Z. Size-Matched Dicarboxylic Acid for Buried Interfacial Engineering in High-Performance Perovskite Solar Cells. *Chem. Eng. J.* **2023**, *460* (15), 141705.
(28) Ji, X.; Bi, L.; Fu, Q.; Li, B.; Wang, J.; Jeong, S. Y.; Feng, K.; Ma, S.; Liao, Q.; Lin, F. R.; Woo, H. Y.; Lu, L.; Jen, A. K. Y.; Guo, X. Target Therapy for Buried Interface Enables Stable Perovskite Solar Cells with 25.05% Efficiency. *Adv. Mater.* **2023**, *35* (39), 2303665.
(29) Chen, J.; Zhao, X.; Kim, S. G.; Park, N. G. Multifunctional Chemical Linker Imidazoleacetic Acid Hydrochloride for 21% Efficient and Stable Planar Perovskite Solar Cells. *Adv. Mater.* **2019**, *31* (39), 1902902.
(30) Zhou, Z.; Liang, J.; Zhang, Z.; Zheng, Y.; Wu, X.; Tian, C.; Huang, Y.; Wang, J.; Yang, Y.; Sun, A.; Chen, Z.; Chen, C. C. Direct In Situ Conversion of Lead Iodide to a Highly Oriented and Crystallized Perovskite Thin Film via Sequential Deposition for 23.48% Efficient and Stable Photovoltaic Devices. *ACS Appl. Mater. Interfaces* **2022**, *14* (44), 49886−49897.
(31) Wu, G.; Li, H.; Cui, J.; Zhang, Y.; Olthof, S.; Chen, S.; Liu, Z.; Wang, D.; Liu, S. Solvent Engineering Using a Volatile Solid for Highly Efficient and Stable Perovskite Solar Cells. *Adv. Sci.* **2020**, *7*, 1903250.
(32) Max, J. J.; Chapados, C. Infrared Spectroscopy of Aqueous Carboxylic Acids: Comparison between Different Acids and Their Salts. *J. Phys. Chem. A* **2004**, *108* (16), 3324−3337.
(33) Gowda, A.; Seo, J.; Ranaweera, C. K.; Babu, S. V. Cleaning Solutions for Resmoval of 30 nm Ceria Particles from Proline and Citric Acid Containing Slurries Deposited on Silicon Dioxide and Silicon Nitride Surfaces. *ECS J. Solid State Sci. Technol.* **2020**, *9* (4), 044013.
(34) Jiang, Q.; Chu, Z.; Wang, P.; Yang, X.; Liu, H.; Wang, Y.; Yin, Z.; Wu, J.; Zhang, X.; You, J. Planar-Structure Perovskite Solar Cells with Efficiency beyond 21%. *Adv. Mater.* **2017**, *29* (46), 1703852.
(35) Jiang, Q.; Zhang, L.; Wang, H.; Yang, X.; Meng, J.; Liu, H.; Yin, Z.; Wu, J.; Zhang, X.; You, J. Enhanced Electron Extraction Using SnO_2 for High-Efficiency Planar-Structure $HC(NH_2)_2PbI_3$-Based Perovskite Solar Cells. *Nat. Energy* **2017**, *2*, 16177.
(36) Zhao, Y.; Ma, F.; Qu, Z.; Yu, S.; Shen, T.; Deng, H. X.; Chu, X.; Peng, X.; Yuan, Y.; Zhang, X.; You, J. Inactive $(PbI_2)_2RbCl$ Stabilizes Perovskite Films for Efficient Solar Cells. *Science.* **2022**, *377* (6605), 531−534.
(37) Dai, Z.; Yadavalli, S. K.; Chen, M.; Abbaspourtamijani, A.; Qi, Y.; Padture, N. P. Interfacial Toughening with Self-Assembled Monolayers Enhances Perovskite Solar Cell Reliability. *Science.* **2021**, *372* (6542), 618−622.
(38) Bi, C.; Wang, Q.; Shao, Y.; Yuan, Y.; Xiao, Z.; Huang, J. Non-Wetting Surface-Driven High-Aspect-Ratio Crystalline Grain Growth for Efficient Hybrid Perovskite Solar Cells. *Nat. Commun.* **2015**, *6*, 7747.
(39) Li, B.; Shi, J.; Lu, J.; Tan, W. L.; Yin, W.; Sun, J.; Jiang, L.; Jones, R. T.; Pigram, P.; McNeill, C. R.; Cheng, Y. B.; Jasieniak, J. J. Facile Deposition of Mesoporous PbI_2 through DMF:DMSO Solvent Engineering for Sequentially Deposited Metal Halide Perovskites. *ACS Appl. Energy Mater.* **2020**, *3* (4), 3358−3368.
(40) Parratt, L. G. Surface Studies of Solids by Total Reflection of X-Rays. *Phys. Rev.* **1954**, *95* (2), 359−369.
(41) Ren, J.; Liu, T.; He, B.; Wu, G.; Gu, H.; Wang, B.; Li, J.; Mao, Y.; Chen, S.; Xing, G. Passivating Defects at the Bottom Interface of Perovskite by Ethylammonium to Improve the Performance of Perovskite Solar Cells. *Small* **2022**, *18* (47), 2203536.

https://doi.org/10.1021/acsenergylett.4c00386
ACS Energy Lett. 2024, 9, 2659−2669

(42) Tolan, M. X-Ray Scattering from Soft-Matter Thin Films. In *Springer Tracts in Modern Physics*; Springer: Berlin, Germany, 1999.
(43) Qin, M.; Chan, P. F.; Lu, X. A Systematic Review of Metal Halide Perovskite Crystallization and Film Formation Mechanism Unveiled by in Situ GIWAXS. *Adv. Mater.* **2021**, *33* (51), 2105290.
(44) Yang, W. S.; Noh, J. H.; Jeon, N. J.; Kim, Y. C.; Ryu, S.; Seo, J.; Seok, S. Il. High-Performance Photovoltaic Perovskite Layers Fabricated through Intramolecular Exchange. *Science.* **2015**, *348* (6240), 1234−1237.
(45) Liu, W.; Shi, T.; Zhu, J.; Zhang, Z.; Li, D.; He, X.; Fan, X.; Meng, L.; Wang, J.; He, R.; Ge, Y.; Liu, Y.; Chu, P. K.; Yu, X. PbI_2-DMSO Assisted in Situ Growth of Perovskite Wafers for Sensitive Direct X-Ray Detection. *Adv. Sci.* **2023**, *10* (1), 2204512.
(46) Ahn, N.; Son, D. Y.; Jang, I. H.; Kang, S. M.; Choi, M.; Park, N. G. Highly Reproducible Perovskite Solar Cells with Average Efficiency of 18.3% and Best Efficiency of 19.7% Fabricated via Lewis Base Adduct of Lead(II) Iodide. *J. Am. Chem. Soc.* **2015**, *137* (27), 8696−8699.
(47) Lee, J. W.; Kim, H. S.; Park, N. G. Lewis Acid-Base Adduct Approach for High Efficiency Perovskite Solar Cells. *Acc. Chem. Res.* **2016**, *49* (2), 311−319.
(48) Many, A.; Rakavy, G. Theory of Transient Space-Charge-Limited Currents in Solids in the Presence of Trapping. *Phys. Rewiew* **1962**, *126* (6), 1980−1988.
(49) Chiu, F. A Review on Conduction Mechanisms in Dielectric Films. *Adv. Mater. Sci. Eng.* **2014**, *2014*, 578168.

https://doi.org/10.1021/acsenergylett.4c00386
ACS Energy Lett. 2024, 9, 2659−2669